Direct numerical simulation of an iron rain in the magma ocean

Hiroki Ichikawa, Stéphane Labrosse, Kei Kurita

JOURNAL OF GEOPHYSICAL RESEARCH, VOL. 115, B01404, doi:10.1029/2009JB006427, 2010

Direct numerical simulation of an iron rain in the magma ocean

H. Ichikawa,[1,2] S. Labrosse,[1] and K. Kurita[3]

Received 3 March 2009; revised 30 July 2009; accepted 17 September 2009; published 29 January 2010.

[1] Core formation in terrestrial planets is a complex process, possibly involving several mechanisms. This paper presents a direct numerical simulation of one of these, the separation of an emulsion of metal in a magma ocean. The model, using a fully Lagrangian approach called the moving particle semi-implicit method, solves the equations of fluid dynamics, including a proper treatment of surface tension. It allows investigation of the balances controlling the distribution of drop size and velocity, in both two- and three-dimensional situations. A scaling analysis where buoyancy is balanced by both surface tension and inertia correctly predicts the average values in these quantities. The full calculation gives an average drop radius of 1.5 cm falling at a velocity of about 30 cm s^{-1}. Analysis of the full distribution remains interesting and shows that a significant part of the smallest droplets is entrained upward by the return flow in molten silicate and might be entrained by succeeding thermal convection. In addition, we investigate the conversion of gravitational energy into viscous heating and the thermal equilibration between both phases. We find that viscous heating is essentially produced at the surface of iron drops and that thermal equilibration is dominated by advection. Scaling thermal diffusion to chemical diffusion leads to the estimation that the latter would happen in less than 100 m in the magma ocean.

Citation: Ichikawa, H., S. Labrosse, and K. Kurita (2010), Direct numerical simulation of an iron rain in the magma ocean, *J. Geophys. Res.*, *115*, B01404, doi:10.1029/2009JB006427.

1. Introduction

[2] The processes leading to the differentiation of the Earth in a silicate mantle and a metallic core have been discussed in several papers [e.g., *Stevenson*, 1990; *Tonks and Melosh*, 1990; *Karato and Rama Murthy*, 1997; *Rubie et al.*, 2003], but owing to the enormous challenges self-consistent treatments represent, the dynamics involved was until recently only sketched. All the proposed scenarios require melting of the metallic part, whereas the silicate part can be solid or liquid. If the silicate stays solid, the segregation can happen by porous flow and compaction of the silicate matrix [e.g. *Stevenson*, 1990; *Yoshino et al.*, 2003; *Bruhn et al.*, 2000], large scale diapirs [*Stevenson*, 1990; *Honda et al.*, 1993; *Samuel and Tackley*, 2008], hydraulic fracturing [*Stevenson*, 2003], or a combination of several of these processes [*Golabek et al.*, 2008; *Ricard et al.*, 2009]. In the case where the silicates are liquid as well, both liquids are assumed to be nonmiscible and to form an emulsion. The large density difference renders the emulsion unstable and leads to a rain of iron in the magma ocean.

[3] All these processes are equally likely and may all have occurred at different stages of planetary formation and at different depth of large planets like the Earth (Figure 1). In particular, the huge energy brought in by the giant impact that formed the Moon is likely to have melted a large fraction of the proto-Earth [*Tonks and Melosh*, 1993; *Canup*, 2004], forming a magma ocean at its surface. Direct evidences in support of this magma ocean are scarce, mostly because they have been largely erased by subsequent convection in the solid mantle. Nevertheless, several arguments can be used in support of this scenario. The existence of positive anomalies in ^{142}Nd in Isua [*Caro et al.*, 2003; *Boyet et al.*, 2003; *Caro et al.*, 2005] requires an significant amount of melting at very early stages of the history of the Earth. The present heat loss of the Earth can be used to constrain its thermal evolution and leads to a hot start, that can be linked to an early magma ocean stage [*Jaupart et al.*, 2007; *Labrosse and Jaupart*, 2007].

[4] The settling of iron drops in the magma ocean is one of the processes of core formation that need to be investigated. In particular, the small size of the iron drops allows important chemical and thermal exchanges between the two phases. The excess in siderophile elements concentration in the mantle and the absence of fractionation between Ni and Co compared to chondrites have been explained by equilibrium between iron and silicates at a pressure in excess of 20 GPa [*Thibault and Walter*, 1995; *Li and Agee*, 1996;

[1] Laboratoire des sciences de la Terre, École Normale Supérieure de Lyon, Lyon, France.
[2] Now at Geodynamics Research Center, Ehime University, Matsuyama, Japan.
[3] Earthquake Research Institute, University of Tokyo, Tokyo, Japan.

0148-0227/10/2009JB006427$09.00

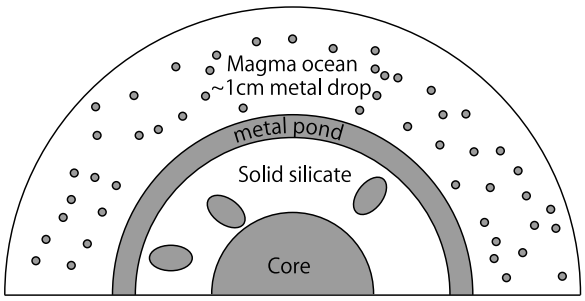

Figure 1. Cartoon of the deep magma ocean model drawn in reference to the work by *Stevenson* [1990], *Rubie et al.* [2003], and *Wood et al.* [2006]. At the surface, magma ocean is formed by release of impact energy and green house effect. Segregated metal droplets in the magma ocean accumulate at the bottom of the magma ocean and forms metal ponds. The metal crosses the solid silicate mantle in the form of diapirs to form the core.

Wood et al., 2006], which corresponds to about 500 km depth in the present Earth. This could very well be explained by chemical equilibrium between millimeter sized iron droplets and liquid silicates near the bottom of a magma ocean before they collect in iron pools too large to allow further equilibration [*Rubie et al.*, 2003].

[5] Core formation as an iron rain in the magma ocean has been modeled only using scaling analysis. In such models, the characteristic size of iron droplets is determined by the balance between different forces, typically the viscous stress that is the cause of drop disruption and surface tension which resists disruption. Whether such scaling apply in the range of parameters relevant to the Earth needs to be tested, which is one of the goals of the present paper. This issue is important since it controls the ability of iron and silicates to equilibrate during the descent of the drops. Indeed, comparison of the time required for a drop to equilibrate to that for crossing any given section of the magma ocean allows identification of the thermodynamic conditions at which the last equilibrium occurred. We expect these scalings to describe rather properly the largest drops in the distribution but what fraction of the total mass does it represent and how does the rest of the distribution behave?

[6] In order to investigate these issues, we developed a fully Lagrangian numerical model solving the dynamics of emulsions under the action of gravity. This allows solution of the time-dependent dynamics of the small scale iron rain in the magma ocean and obtain the statistically steady distributions of sizes and velocity of iron drops. We propose a scaling of the average values of these quantities in the inertial regime and find a fair agreement with the scaling predictions. Analysis of the full distribution implies that some part of the smallest droplets are entrained upward by the return flow in the silicate which could, on a larger scale, bring them to the top of the emulsion where thermal convection in the magma ocean might be able to entrain a small fraction of them.

[7] Thermal equilibration of metal and silicate is studied by solving the energy balance equation together with the momentum balance. It is found to be dominated by advection. A typical time for thermal equilibration is 5 s for a droplet having a radius of 4 mm falling at about 10 cm s^{-1}, which corresponds to a distance of 50 cm. Chemical diffusion being slower than thermal diffusion is even less relevant and chemical equilibration should also be dominated by advection and can be estimated to occur in about 50 m.

2. Equations

[8] In this section, the conservation equations for the two phases are explained, with a particular care in the interfacial aspects. At the scale of interest here (typically about 10 cm), both liquid metal and silicates can be considered as incompressible fluids, so that the mass conservation equation leads:

$$\nabla \cdot \mathbf{u} = 0, \tag{1}$$

u being the velocity. Equation (1) is obviously valid in each phase but also at the interfaces between phases because of the absence of phase change.

[9] In order to write the balance equation for momentum, we need to write the surface tension stresses. These apply only to the surface but it is desirable to write a volume version of it, by introducing a surface Dirac (generalized) function, δ_Σ, which is also the interfacial surface area per unit volume. To that end, we introduce a characteristic function, θ, which takes the value 0 in fluid 0 and 1 in fluid 1. This function is best viewed as a distribution (generalized function) [*Drew*, 1983] and the domain of integration V is either $\mathbb{R}^3$, all functions having the proper decay properties at infinity, or the base cell of a periodic domain.

[10] The volume fraction ϕ of fluid 1 in volume V is simply computed as $\phi = \frac{1}{V}\int_V \theta dV$ and the average of any given quantity q in fluid 1 contained in volume V is $\langle \theta, q \rangle \equiv \langle q \rangle_1 = \frac{1}{V}\int_V q\theta dV$. Now, $\nabla\theta$ essentially provides the quantities pertaining to the interface between the two phases [*Bercovici et al.*, 2001]. More precisely, the Dirac function we seek, δ_Σ, centered on the interface is defined as $\delta_\Sigma \equiv \hat{\mathbf{n}} \cdot \nabla\theta$, with $\hat{\mathbf{n}} = \nabla\theta/\|\nabla\theta\|$ the unit vector normal to the interface, pointing from fluid 0 (metal) to fluid 1 (silicate). Then, the total surface S of interface contained in volume V is simply written: $S = \int_V \delta_\Sigma dV$. Therefore, δ_Σ is the interfacial area per unit volume and has the dimension of 1 m.

[11] The momentum equation including a constant surface tension can then be written as [e.g., *Brackbill et al.*, 1992; *Scardovelli and Zaleski*, 1999]

$$\begin{aligned}\frac{D\mathbf{u}}{Dt} &= -\frac{1}{\rho}\nabla p + \frac{1}{\rho}\nabla \cdot \left\{\eta\nabla\mathbf{u} + \eta(\nabla\mathbf{u})^T\right\} \\ &\quad + \left(\frac{\rho_0}{\rho} - 1\right)g\mathbf{e_z} - \frac{\gamma}{\rho}\hat{\mathbf{n}}(\nabla_\Sigma \cdot \hat{\mathbf{n}})\delta_\Sigma, \\ \text{with}\quad \nabla_\Sigma &= \nabla - \hat{\mathbf{n}}(\hat{\mathbf{n}} \cdot \nabla) \text{ and } p = P - p_0,\end{aligned} \tag{2}$$

where η, P, p_0, **g**, ρ_0, and γ are dynamic viscosity, pressure, hydrostatic pressure, acceleration due to gravity, average density, and interfacial tension coefficient, respectively, and a Newtonian rheology has been assumed. Note that interfacial tension only acts in the normal direction because

Table 1. Representative Parameter Values Used in the Calculations and the Resulting Characteristic Scales and Dimensionless Numbers[a]

Parameter	Value
ρ_s	3750 kg m^{-3}
ρ_m	7800 kg m^{-3}
C_p	10^3 J kg^{-1} K^{-1}
γ	1 N m^{-1}
g	10 m s^{-2}
k_s	3.75 W K^{-1} m^{-1}
k_m	7.8 W K^{-1} m^{-1}
α	6×10^{-5} K^{-1}
$\eta_s = \eta_m$	1 Pa s
L	5 mm
U	0.23 m s^{-1}
τ	0.02 s
Θ	1.24×10^{-5} K
Re_s	4.4

[a]See *Rubie et al.* [2003].

we assume a constant γ. We adopted the hydrostatic balance as a basic state for the calculation

$$\frac{1}{\rho_0}\frac{\partial}{\partial z}p_0(z) = -g \Rightarrow p_0(z,t) = -\rho_0 g z. \tag{3}$$

[12] In order to investigate the partitioning of the gravitational energy between metal and silicate and equilibration between fluids, we solve an energy equation

$$\rho C_p \frac{DT}{Dt} = \nabla \cdot (k\nabla T) + 2\eta \mathbf{E} : \mathbf{E} \tag{4}$$

with T the temperature, C_p the specific heat per unit mass, k the thermal conductivity, and

$$2\eta \mathbf{E} : \mathbf{E} = \frac{\eta}{2}\left(\frac{\partial u_i}{\partial x_j} + \frac{\partial u_j}{\partial x_i}\right)^2$$

the rate of viscous heating. This term is responsible for the transformation of gravitational potential energy into heat. We neglected here the term $\alpha T(DP/Dt)$, often referred to as "adiabatic heating," because its ratio to the viscous heating term is of order $\alpha T\rho/\Delta\rho \sim 0.1$ for a temperature of 2000 K. For the same reason, the temperature dependence of the density is not taken into account in the momentum equation and no feedback of the energy equation on the flow is considered.

[13] Equations (1), (2), and (4) are valid at each position but the physical parameters take different values in the two fluids, denoted by subscript m for metal and s for silicate. In order to reduce the parameter space, it is useful to introduce some dimensionless numbers and to render the balance equations dimensionless as well. Metal and silicates have different physical properties and we use that of the latter, ρ_s, η_s and k_s, as references essentially because the continuous phase is composed of silicate. For the density, another choice could make sense, $\Delta\rho = \rho_m - \rho_s$, since this is at the origin of the driving force. However, in terms of numerical values, $\Delta\rho \simeq \rho_s$ and using ρ_s as reference in all terms helps to simplify the equation. With this choice, the physical parameters have a dimensionless form noted with a star exponent, $\rho^\star = (1 \text{ or } \rho_m/\rho_s)$, and similarly with other physical parameters. Any temperature dependence of the physical quantities, in particular density if thermal convection is to be considered, could be added here.

[14] Then, we seek two scales, length L and velocity U, which provide the timescale by a simple ratio. The buoyancy and interfacial forces are important players in the dynamics and their balance provides the length scale:

$$\rho_s g = \frac{\gamma}{L^2} \quad \Rightarrow \quad L = \sqrt{\frac{\gamma}{\rho_s g}}. \tag{5}$$

This is equivalent to considering the Bond (or Eötvös) number, $Bo = L^2 g\Delta\rho/\gamma$, close to unity. (Remember that $\Delta\rho \simeq \rho_s$.) Note that if the droplets are very small, the interfacial force can only be balanced by pressure (Laplace balance) and the shape of the droplet is essentially spherical.

[15] For the velocity scale U, the previous two terms can be balanced either with the viscous force, leading to a Stokes scaling, or to inertia. The proper choice is dictated by the value of the Reynolds number, $Re = \rho_s UL/\eta_s$, which is not imposed a priori but is an output of the model. We nevertheless expect it to be larger than one, favoring a scaling derived from the balance between inertia and surface tension (or buoyancy):

$$\frac{\gamma}{L} = \rho_s U^2, \tag{6}$$

which is equivalent to assuming a Weber number, $We = \rho_s U^2 L/\gamma$, of order one. Substituting equation (5) into equation (6) leads to $U = \sqrt{gL} = (\gamma g/\rho_s)^{1/4}$. From equations (5), the timescale is $\tau = L/U = (\gamma/\rho_s g^3)^{1/4}$. Finally, using γ/L as pressure scale, equation (2) takes the form

$$\frac{D\mathbf{u}}{Dt} = -\frac{1}{\rho^\star}\nabla p + M^{\frac{1}{4}}\frac{1}{\rho^*}\nabla \cdot \left\{\eta^\star \nabla \mathbf{u} + \eta^\star (\nabla \mathbf{u})^{\mathbf{T}}\right\} + \left(\frac{\rho_0^\star}{\rho^\star} - 1\right)\hat{\mathbf{e}}_\mathbf{z} - \frac{1}{\rho^\star}(\nabla_\Sigma \cdot \hat{\mathbf{n}})\delta_\Sigma \hat{\mathbf{n}}. \tag{7}$$

where all variables are given the same notation as before for simplicity. The Morton number, $M = Re_s^{-4} = \eta_s^4 g/\gamma^3 \rho_s$, with $Re_s = \rho_s UL/\eta_s$ and the Bond number have been used to classify drop shapes [*Clift et al.*, 1978].

[16] Table 1 gives representative values for the different parameters entering the problem and the resulting characteristic scales and dimensionless numbers. Some of these parameters are quite uncertain and most notably the viscosities. The fact that the estimated Reynolds number is slightly larger than one justifies the use of inertia as a scaling factor instead of viscous force. This point will be made stronger by realising that the viscosities used in this calculations are overestimates of the actual silicate viscosity [*Liebske et al.*, 2005]. However, the viscosity could also be influenced by temperature and the presence of crystals and we varied its value between 10^{-2} Pa s and 10 Pa s.

[17] There are mainly three remaining important parameters for the dynamics: M, ρ_m^*, and η_m^*. The uncertainties in density determination of both phases are small and the

Table 2. Input Parameters and Results for the Two-Dimensional Calculations[a]

Case	η_s (Pa s)	η_m (Pa s)	Metal Fraction	Number of Particles	Morton Number	Number of Drops	Radius (m)	Velocity (m s^{-1})	r_{max} (m)	v_{max} (m s^{-1})
A1	0.01	0.01	0.0576	90 000	2.67×10^{-11}	1	0.00383	−0.209	0.00552	−0.263
A2	0.1	0.1	0.0576	90 000	2.67×10^{-7}	1	0.00404	−0.184	0.00578	−0.227
A3	0.5	0.5	0.0576	90 000	1.67×10^{-4}	1	0.00426	−0.110	0.00579	−0.193
A4	1.0	1.0	0.0576	160 000	2.67×10^{-3}	1	0.00421	−0.108	0.00659	−0.197
A5	1.0	1.0	0.0576	160 000	2.67×10^{-3}	256	0.00409	−0.108	0.00625	−0.188
A6	2.0	2.0	0.0576	90 000	4.27×10^{-2}	1	0.00533	−0.105	0.00836	−0.168
A7	5.0	5.0	0.0576	40 000	1.67	4	0.00748	−0.118	0.00976	−0.139
A8	10.0	10.0	0.0576	40 000	2.67×10	4	0.00946	−0.0748	0.0114	−0.0893
B1	0.01	0.01	0.18	90 000	2.67×10^{-11}	1	0.00593	−0.107	0.00970	−0.131
B2	0.1	0.1	0.18	90 000	2.67×10^{-7}	1	0.00564	−0.101	0.00900	−0.147
B3	0.5	0.5	0.18	90 000	1.67×10^{-4}	1	0.00505	−0.0711	0.00844	−0.148
B4	1.0	1.0	0.18	90 000	2.67×10^{-3}	1	0.00493	−0.0654	0.00854	−0.166
B5	2.0	2.0	0.18	90 000	4.27×10^{-2}	1	0.00518	−0.0674	0.00939	−0.166
B6	5.0	5.0	0.18	40 000	1.67	4	0.00774	−0.0802	0.0140	−0.175
B7	10.0	10.0	0.18	40 000	2.67×10	4	0.0102	−0.0819	0.0161	−0.130
B8	10.0	1.0	0.18	40 000	2.67×10	4	0.00956	−0.0991	0.0159	−0.149
C1	2.0	2.0	0.025	90 000	4.27×10^{-2}	1	0.00892	−0.261	0.00892	−0.261
C2	2.0	2.0	0.03	90 000	4.27×10^{-2}	1	0.00977	−0.286	0.00977	−0.286
C3	2.0	2.0	0.035	90 000	4.27×10^{-2}	1	0.00782	−0.248	0.00913	−0.252
C4	2.0	2.0	0.040	90 000	4.27×10^{-2}	1	0.00662	−0.160	0.00895	−0.235
D1	1.0	10.0	0.0576	90 000	2.67×10^{-3}	1	0.00440	−0.112	0.00672	−0.179

[a]Number of drops refers to the initial number of metal droplets; r_{max} and v_{max} are the time averages of radius and velocity of the largest droplet.

density ratio ρ_m^* can be set to a constant value. On the other hand, the viscosities are not well constrained and we can therefore vary both viscosities as control parameters or vary their ratio and the Morton number.

3. Numerical Method

[18] In order to solve the partial differential equations discussed in section 2, we use the moving particle semi-implicit (MPS) method [*Koshizuka and Oka*, 1996], which is Lagrangian and well suited for incompressible flows. Lagrangian methods allow natural tracking of interfaces, which make them the ideal choice to study the dynamics of an emulsion. It has already been used to model various fluid flows, such as free surface flow [*Koshizuka and Oka*, 1996], multiphase flow [*Nomura et al.*, 2001], and flow including phase change [*Koshizuka et al.*, 1999]. In order to treat the surface tension term within MPS, the curvature is needed and we use the method proposed by *Nomura et al.* [2001] for two-dimensional (2-D) problems and that developed by *Ichikawa and Labrosse* [2010] for three-dimensional (3-D) problems. In two dimensions, the curvature is computed by fitting a circle on the interface whereas in three dimensions, it is computed as $\nabla_\Sigma \cdot \hat{\mathbf{n}}$, where the normal vector is obtained from the gradient of the color function using a blending of MPS and smooth particle hydrodynamics (SPH). We do not use any special algorithm to treat coalescence, as would be required for a precise study of that phenomenon, because the small viscosities considered here render that process very fast [*Eggers et al.*, 1999] compared to the typical velocity of the fluid. In our model, merging happens naturally when two drop surfaces get within range of particle interaction and we think this treatment is sufficient to deal with the global characteristics if the emulsion.

[19] The computational domain has periodic boundaries in all directions, vertical as well as horizontal. In two dimensions, the computational particles are initially placed in a square lattice whereas in three dimensions, we use a hexagonal close-packed structure for the initial particle allocation. Such choices have little influence on the dynamics after the initial transient phase.

[20] We computed cases with volume fraction of metal, $\phi = V_m/(V_m + V_s)$, equal to 0.18 and 0.0576 and a few cases with a lower value. Unless otherwise stated, there is initially only one droplet, at rest, with a square shape. Square drops rapidly lose their initial shape by the effect of surface tension and after a few cycles of disrupting and merging, the initial condition is totally forgotten. We also considered, as initial condition, the case of many droplets evenly spaced. The silicate viscosity is varied from 10^{-2} Pa s to 10 Pa s in the 2-D calculations, corresponding to a temperature of ∼2800 to ∼1700 K [*Rubie et al.*, 2003, Figure 2b].

4. Results

4.1. Overview of Two-Dimensional Calculations

[21] In two-dimensional calculations, one or more square droplets are initially set at rest. All parameter sets are listed in Table 2. The computational domain is 10 cm × 10 cm or, in dimensionless form, 19.4 × 19.4. We computed solutions for $\eta_s = \eta_m$ = 0.01,0.1,0.5,1.0,2.0,5.0, and 10.0 Pa s for two different volume fractions of metal, 5.76% (cases A1–A8 and D1) and 18.0% (cases B1–B8). We also computed solutions for η_m/η_s = 0.1 with η_s = 10.0 Pa s for a volume fraction of metal of 18.0% (case B8). In terms of resolution, we used 40,000 particles for $\eta_s \geq$ 5.0 Pa s, and 90,000 particles for all other calculations, except for the cases A4 and A5 with $\eta_s = \eta_m$ = 1.0 Pa s and a metal fraction of 5.76% for which we used 160,000 particles. The particles are initially set at rest on a square lattice.

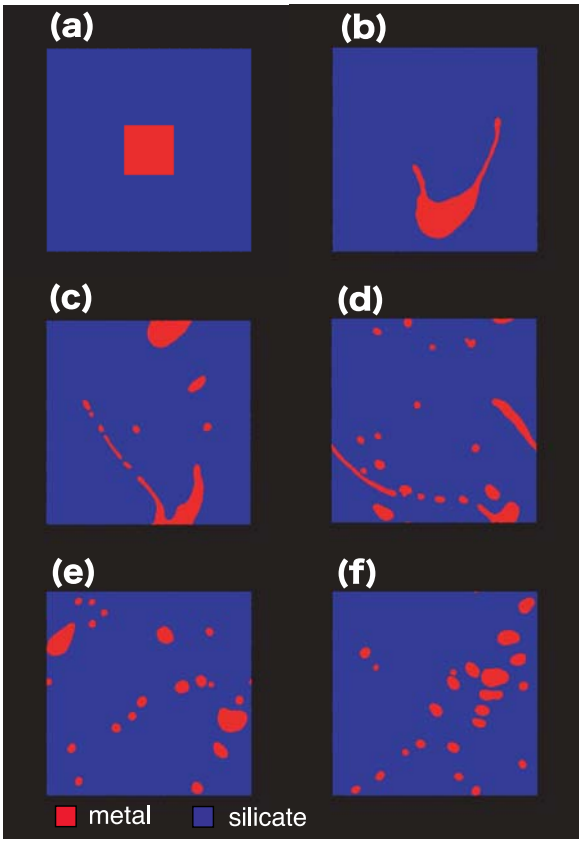

Figure 2. Case A4. Falling metal droplet in silicate liquid. Boundaries are periodic in all directions. An initially square drop is deformed into a boomerang shape and broken up by the viscous stress. The times of the different frames are (a) 0 s, (b) 0.52 s, (c) 0.8 s, (d) 1.2 s, (e) 2.0 s, and (f) 10 s (see Table 2 for a full list of parameters). Movie 1 is also for this case.

[22] Let first discuss in details the cases with $\eta_s = \eta_m =$ 1.0 Pa s and a metal fraction of 5.76% using 160,000 particles. Two different initial conditions are considered: case A4 with only one large metal drop (Figure 2) and case A5 with 256 droplets originally set in a lattice arrangement (Figure 3). The gravity force is directed toward the bottom of Figures 2 and 3. In case A4, the drop gets first elongated by the viscous stress exerted by the ambient fluid and takes the shape of a boomerang (Figure 2b). After about 0.5s, the viscous stress overcomes surface tension and the droplet is disrupted into several droplets. A statistically steady state is reached after about 2 s. In case A5, the lattice-like arrangement collapses (Figure 3b) and droplet sizes increase by repeated merging (Figures 3b–3e). Finally, the very small droplets in Figure 3e are swept in by larger drops and the system reaches a statistically steady state identical to the one reached in case A4. The time to reach that state is, however, longer, of the order of 10s. In the statistically steady state, the system keeps its droplet size distribution by compensating merging and disruptions.

[23] Figure 4 shows the time dependence of the average drop size and velocity for the two cases. The average velocity is defined as the arithmetic average over all the metal particles, which is equivalent to a mass or volume average among all drops since the fluid is considered as incompressible. We can see that the average velocity of the metal phase fluctuates with time, and so must also be the case of the average silicate velocity.

[24] The effective radius r of a droplet is computed from its volume V by assimilating the droplet to a disk. The mean radius is then obtained by volume weighted average, $\sum_i r_i V_i / \sum_i V_i$, where the sum is taken over the droplets. The time sequence of the mean of droplets' radii and velocity (Figure 4) show that case A4 reaches steady state faster than case A5. In case A5, if a drop is slightly larger than the neighboring ones, its higher velocity will make it catch the drops that are in front and merge with them which will make its advantage even bigger. *Stevenson* [1990] showed, using a simple model for the growth of this larger drop, that the time required to reach the maximum size is very small.

[25] We already showed that the average size and velocity of the droplets are independent of the initial condition, either starting with only one large drop or with a set of small ones. We can now go one step further and compare their size distribution, as represented on Figure 5. Both distributions represent the time and space variability once a statistically steady state has been reached. They are identical and show the sharply defined minimum of droplet sizes a

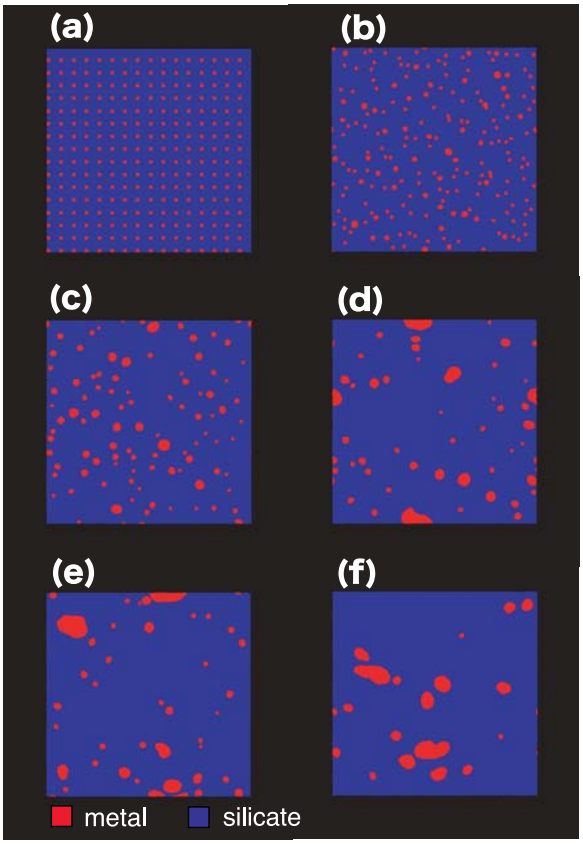

Figure 3. Case A5. Falling metal droplets in silicate liquid. The boundaries are periodic in all directions. Two hundred and fifty-six initially square drops are placed at lattice points. The times for the different frames are (a) 0 s, (b) 1.0 s, (c) 4.0 s, (d) 8.0 s, (e) 10.0 s, and (f) 32.0 s (see Table 2 for a full list of parameters).

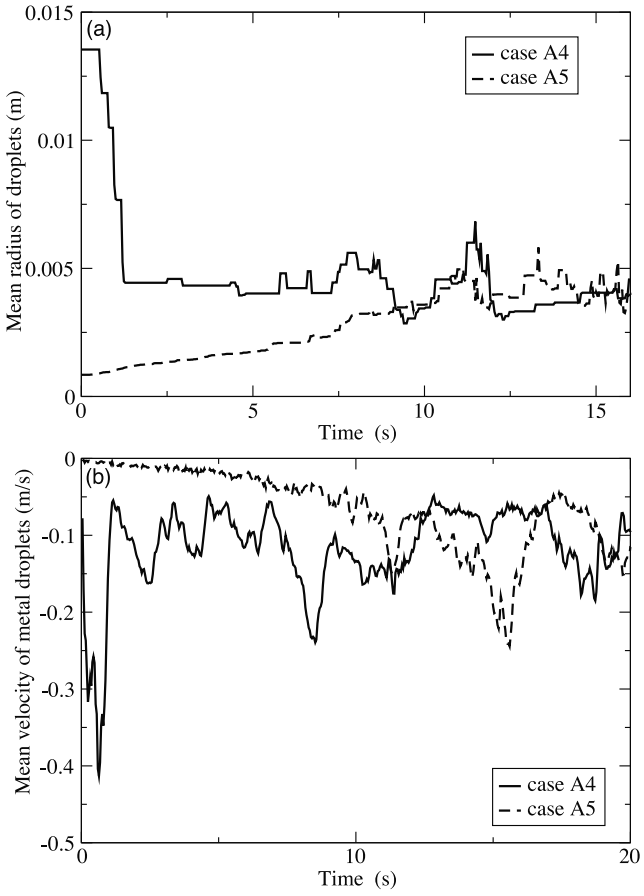

Figure 4. Mean (a) radius and (b) velocity of the metal droplets in the two-dimensional case with $\eta_s = \eta_m = 1$ Pa s. The two cases are statistically identical after about 10 s. In case A4, the initial condition has only one square drop (Figure 2). I case A5, the initial condition has 256 square droplets (Figure 3).

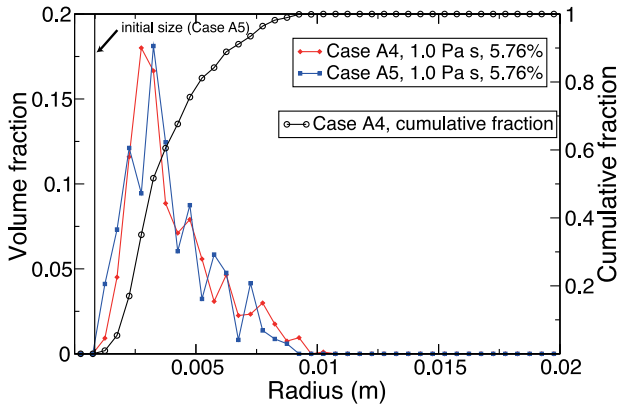

Figure 5. Comparison of the size distributions of droplets, in volume fraction of the total for cases A4 and A5 in statistically steady state. The distributions represent both temporal and spatial variations. The cumulative distribution for case A4 is also shown. The lowest size in the distribution is similar to the initial size of droplets in case A5, as shown by the vertical line.

little more than ~0.001 m, and a long tail toward the large values of droplet sizes. Smaller droplets that exist originally for case A5 are rapidly swept by bigger ones. Droplets smaller than that minimum cannot be formed by disruption of bigger ones because it requires a very large viscous force to counteract the surface tension in droplets with such small radius of curvature.

[26] The survival time of initial small droplets is short, about 20 s in the simulation, which would be dependent on the initial size, much shorter than the total falling time in the magma ocean. Therefore, we hereafter concentrate the analysis on the properties of droplets in steady state.

4.1.1. Dependence on Viscosity or Morton Number

[27] The mean radius and velocity of droplets, averaged in time once a statistically steady state has been reached, are presented on Figure 6 for different values of the silicate viscosity. The Morton number and the dimensionless radius

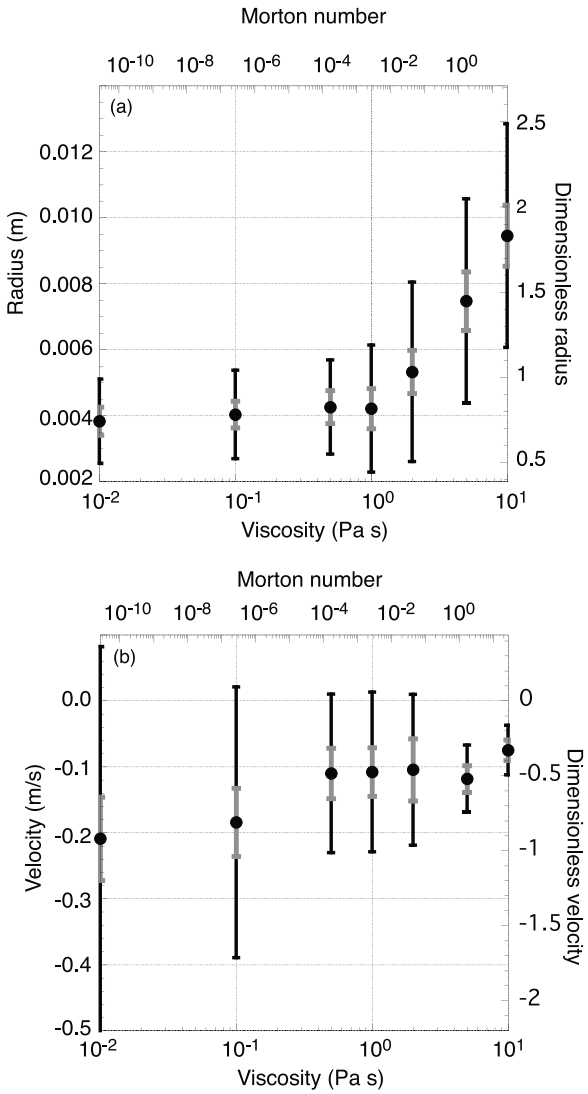

Figure 6. Variation of the mean droplet (a) radius and (b) velocity as function of silicate viscosity or Morton number for a volume fraction $\phi = 0.0576$. Light grey error bars denote the standard deviation with time of the mean value. Black error bars denote the standard deviation of the full distribution.

Table 3. Input Parameters and Results for the Three-Dimensional Calculations[a]

Case	Metal Fraction	L_x (m)	L_y (m)	L_z (m)	Number of Particles	Number of Drops	Radius (m)	Velocity (m s^{-1})
3D1	0.0576	0.0593	0.0595	0.120	244 596	1	0.0159	−0.261
3D2	0.0576	0.0593	0.0595	0.120	244 596	64	0.0159	−0.283
3D3	0.18	0.0593	0.0595	0.120	244 596	1	0.0221	−0.195
3D4	0.0576	0.0902	0.0900	0.120	562 331	1	0.0145	−0.279

[a]L_i denotes the length of the domain for each direction (x, y, z). Number of drops stands for the initial number of metal droplets.

and velocity are also given on the graph. One can see that, with increasing viscosity, the average size increases and the average velocity decreases. However, the increase in droplet size with viscosity is very small for $\eta_s \leq 1.0$ Pa s and then transitions to another regime where it increases rapidly. This transition can be associated to a transition from high Reynolds number to low Reynolds number regime. At the transition, with a viscosity of about ~1 Pa s (Figure 6), the Reynolds number estimated from the average size and velocity of drops is $Re = 1.7$, of the same order as the value estimated earlier from the scaling analysis ($Re = 4.4$). In the case of large Re, the viscosity ceases to play a role, even though the smallest droplets have a low Reynolds number. This validates the previous analysis (equation (5)) where the size of droplets was predicted independently of the viscosity. On the other hand, the large increase of drop size in the high viscosity regime requires a different scaling analysis to be explained.

[28] The estimated length scale is derived from equating gravity force, drag force and surface tension acting on a drop. The breakup by the action of the viscous force should lead to a different scaling. Following *Stevenson* [1990], one can assume a Stokes velocity $v \sim g\Delta\rho R^2/\eta_s$ and balance viscous stress $\eta_s v/R$ with surface tension γ/R to get a limit radius of $R \sim \sqrt{\gamma/g\Delta\rho}$. However, this scaling is independent of the viscosity which cannot explain Figure 6. This scaling only provides a maximum size and bigger drops should be unstable. However, the time required for the instability to fully develop and decrease the drop size back to a stable situation is not specified.

[29] It would be interesting to extend the present results to higher viscosities to see whether the sizes stabilizes to a definite high viscosity size. However, these calculations are more time consuming because of the smaller time steps and the larger computational domains required, which limited our investigations.

4.1.2. Effect of the Volume Fraction of Metal

[30] We modeled situations with two different volume fractions ϕ of metal, 5.76% and 18%, and the different results are summarized in Tables 2 and 3. The main effect of increasing the metal fraction is to increase the size of the drops and decrease their velocity. This results from the form of the buoyancy force (equation (2)) in which the average density ρ_0 increases with the fraction of metal, and the relative buoyancy of each metal particle therefore decreases. The decrease of the driving force with ϕ leads to a decrease of the velocity and therefore of the viscous drag. This allows the drop size to increase.

4.1.3. Effect of the Viscosity Ratio

[31] The viscosity of the metallic phase plays little role as long as it is smaller than that of the silicate. Table 2 shows the average radius and velocity of the metal phase for several cases with different viscosity ratios, $\eta_s/\eta_m = 10$, 1, and 0.1, and they do not show any marked difference. Because the silicate phase is more abundant and, more importantly, connected, its viscosity influences more effectively the dynamics.

4.1.4. Viscous Heating in Two-Dimensional Calculations

[32] Once a statistical steady state is reached concerning the distributions in drop sizes and velocities, the gravitational energy released by the net downflow of mass is entirely converted in viscous heating. In the model, this can be seen by integrating equation (4) over the computational domain, using its periodicity. In order to link this to the gravitational energy, consider the equation for conservation of total energy, $\epsilon = e + u^2/2$, with e the internal energy and $u^2/2$ the kinetic energy:

$$\frac{d}{dt}\int_V \rho\epsilon dV = -\int_V \nabla\cdot\mathbf{q}dV + \int_V \rho\mathbf{g}\cdot\mathbf{u}dV + \int_V \nabla\cdot(\boldsymbol{\sigma}\cdot\mathbf{u})dV, \tag{8}$$

with $\boldsymbol{\sigma}$ the total stress tensor, which can be decomposed in a hydrostatic part and the rest: $\sigma_{ij} = -p_0\delta_{ij} + \tau_{ij}$. Using the periodicity of the computational domain, both the heat flux and $\boldsymbol{\tau}$ terms drop. The second term on the right hand side is also null from mass conservation and an uniform $\mathbf{g}$, and we are left with

$$\frac{d}{dt}\int_V \rho\epsilon dV = -\int_S p_o\mathbf{u}\cdot\mathbf{dS}. \tag{9}$$

Only the horizontal surfaces contribute to this integral and the result depends on the gradient of the hydrostatic pressure. Let introduce the average vertical velocity of the metal u_m and silicate u_s, which are linked by mass conservation:

$$\phi\rho_m u_m + (1-\phi)\rho_s u_s = 0. \tag{10}$$

In statistical steady state, the kinetic energy is constant and equation (8) leads to an equation for the evolution of the average temperature T_0 using the periodicity of the computational domain:

$$\frac{dT_0}{dt} = \frac{g}{C_p}\left(1 - \frac{\rho_m}{\rho_s}\right)\phi u_m. \tag{11}$$

This leads to a steady increase in the temperature, and Figure 7 shows the evolution of the mean temperature in each phase as a function of time, along with the predicted slope from equation (11).

[33] In addition, Figure 7 allows the study of the thermal equilibration of the two phases. Before discussing that part,

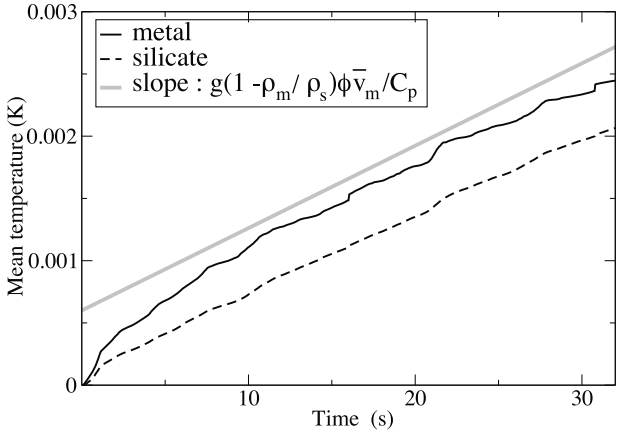

Figure 7. Mean temperature of metal (solid line) and silicate (dashed line) in a two-dimensional calculation (case A4) with $\eta_s = \eta_m = 1.0$ Pa s. The solid gray line shows the temperature increase rate predicted by computing the gravitational energy release (see details in the text).

it is worth considering where viscous heating actually occurs. Figure 8 shows that viscous dissipation occurs mostly at the interface between phases. Since thermal diffusivity is identical in both phases, each should benefit equally, but Figure 7 shows that, on the contrary, the average temperature is larger in the metal than in the silicate. This simply is explained by the metal phase having a larger surface to volume ratio than the silicate.

[34] This initial difference is counteracted by advection and diffusion, and in steady state, the case represented on Figure 7 predicts a remaining difference of about 4×10^{-4} K. Also, the time difference between the two curves, about 5 s, can tell us what is the main mechanism for equilibration. Indeed, a 4 mm drop equilibrates thermally by diffusion in about $R^2/\kappa \sim 16$ s, which is larger than obtained in the calculation. On the other hand, the velocity being about 0.1 m s^{-1}, the advection timescale is around 4×10^{-2} s and explains the very small difference in temperature between the two phases.

4.2. Three-Dimensional Simulations

[35] Since collisions between metal droplets play an important role one may consider that the dimensionality of the calculation has a strong influence on the results. We have performed three-dimensional calculations, in which one or more metal droplets with an initially cubic shape are set at rest in the liquid silicate and their subsequent evolution is computed. These calculations are of course more time consuming than their two-dimensional counterpart which limited the exploration of the parameter space. All calculations used a domain that was longer in the vertical direction than in the horizontal one and the viscosities are $\eta_s = \eta_m = 1$ Pa s. Two different volume fractions were used, 5.76% and 18%, and all other parameters are given in Table 3.

[36] Figure 9 shows the evolution of the metal phase (volume fraction $\phi = 5.76\%$) initially set as only one cubic drop, for two different domain horizontal size (cases 3D1 and 3D4). Corresponding Movies 1–3 show that the drop first gets a spherical shape to remove the singularities of the initial cubic shape.[1] Then, the flow in the silicate phase around the drop drives a flow inside the drop and provokes an indentation on the top of the metal drop while elongating the sides (Figure 10). Small droplets separate from the edges of this spherical cap. This is quite similar to the dynamics obtained in two-dimensional calculations as displayed in Figure 2.

[37] We also computed the case with initially 64 cubic droplets, all other parameters being the same as the case just discussed, including the volume fraction of metal. The evolution of the metal phase is displayed in Figure 11. After a transient period that involves the successive merging of droplets, the system reaches a statistically steady state similar to the case starting with a large drop. The situation is similar to the discussion in two-dimensional calculations and the time required to reach the steady state is much longer when starting with small droplets.

4.3. Comparison Between Two- and Three-Dimensional Results and Scaling Predictions

[38] The dimensional analysis presented above (section 2) makes no distinction between two-dimensional (2-D) and three-dimensional (3-D) analysis. We find that the prediction from this dimensional analysis are close to the result of both the 2-D and the 3-D calculations. For example, using $\eta_s = \eta_m = 1$ Pa s, the scaling predicts a drop radius (equation (5)) of $L = 5 \times 10^{-3}$ m and a velocity of $V = -2.3 \times 10^{-1}$ m s^{-1}. The 3-D calculation (case 3D4) gives (Table 3) $R_{3D} = 1.45 \times 10^{-2}$ m and $V_{3D} = -2.79 \times 10^{-1}$ m s^{-1} for mean radius and velocity, respectively, whereas the 2-D calculation (case A4) gives (Table 2) $R_{2D} = 4.2 \times 10^{-3}$ m and $V_{2D} = -1.08 \times 10^{-1}$ m s^{-1}. One can think of several geometrical effects to explain the slight differences. First, a 2-D drop is in fact an infinite cylinder with a lower surface over volume ratio than a 3-D drop with the same radius. This favors, in two dimensions, volumetric terms in the momentum equation (inertia and buoyancy force) over the surface term (interfacial tension), and therefore leads to drops that are 50% smaller than their 3-D counterpart. Moreover, the mean curvature in two dimensions is $1/R$ and is therefore half the value in three dimensions, which reinforces this prediction.

[39] We constructed probability charts in the (R, V) space, for both 2-D and 3-D calculations (Figure 12) in order to test a simple relationship between drop size and velocity. To first order, both distributions are similar: the fastest drops (that having the largest absolute value of their velocity) are the largest ones, and vice versa. In both cases, the smallest drops have a positive velocity, meaning that they move upward. In fact, they are entrained by the silicate flow that moves opposite to the metal flow in order to conserve mass. The energy necessary to create these small droplets comes from the gravitational settling of the largest drops that is responsible for the largest stresses.

[40] There are also differences between the two distributions. First, the correlation between the radius and velocity is more clearly defined in three dimensions than in two dimensions. In particular, the 2-D calculation has some small droplets that fall faster than the bigger ones and this

[1] Animations are available in the HTML.

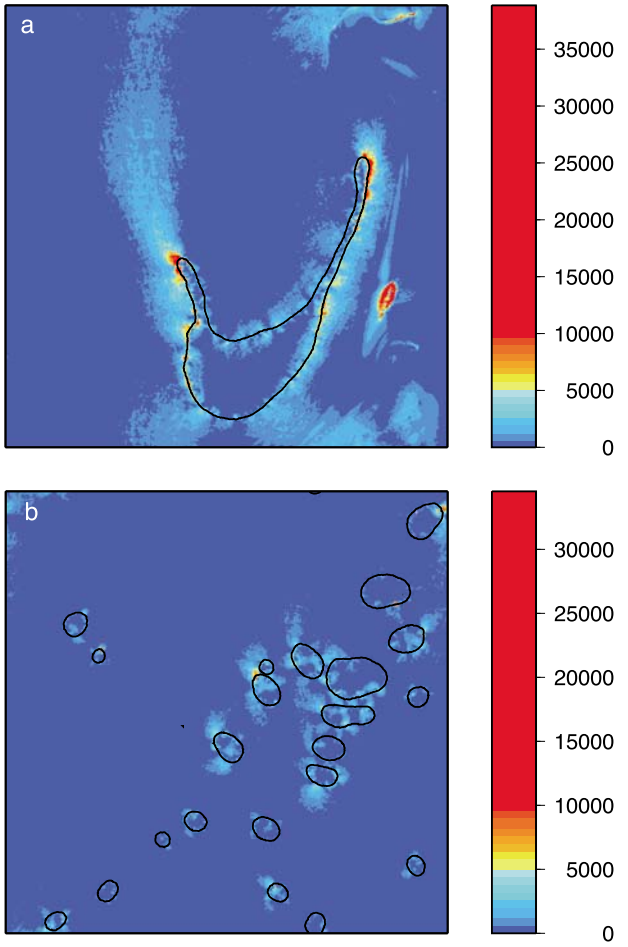

Figure 8. Viscous dissipation (in W m^{-3}) in a 2-D calculation at two different times, corresponding to Figures 2b and 2f. One can see that viscous dissipation mostly occurs at the interface between phases.

is responsible for a large part of the scatter in the distribution. Again, inspection of Movies 1–3 provides an explanation: When a small droplet is formed at the rear of a large one, it can get entrained in its wake and gets accelerated. The same situation may arise in three dimensions but the small droplets have more options of escaping from the influence of the large drop than in two dimensions, which limits this effect. Another important difference between the two cases lies in the clear bimodal nature of the distribution obtained in three dimensions compared to the unimodal one obtained in two dimensions.

[41] To conclude this section, we would like to stress that the results from two- and three-dimensional calculations both agree with the scaling analysis presented above when dealing with the average velocity and size of drops in the inertial regime. This justifies the use of a two-dimensional setup to explore the phase space. However, to go beyond these gross characteristics and deal with full distributions, three-dimensional models are required.

5. Discussion

[42] After having presented the raw results, it is worth discussing their physical meaning. The implications for the dynamics of an iron rain in the magma ocean will be outlined, with a particular concern on equilibration processes and the possibility of iron residues in the mantle.

[43] In the magma ocean, the effective conditions of equilibration depend on the average size of drops, about 1 cm in our calculation, which is similar to the value proposed by *Rubie et al.* [2003]. Moreover, the study of thermal equilibration, discussed in section 4.1.4, reveals the importance of convective transfer in the drops, which enhances the equilibration rate compared to a purely diffusive process. This means that the average drop continuously equilibrates with the surrounding magma as it falls, with negligible delay. In the case discussed in section 4.1.4, thermal equilibrium is reached in about 5 s, which corresponds to a distance of about 50 cm. Of course, in the case of chemical equilibrium, diffusion across the metal-silicate interface is less efficient and equilibration would take longer. Assuming a diffusion coefficient $D = 10^{-8}$ m^2 s^{-1} [*Rubie et al.*, 2003], which is a hundred times lower than the thermal diffusion coefficient, a distance of about 50 m would be obtained, similar to the distance proposed by *Rubie et al.* [2003]. This means that the equilibrium

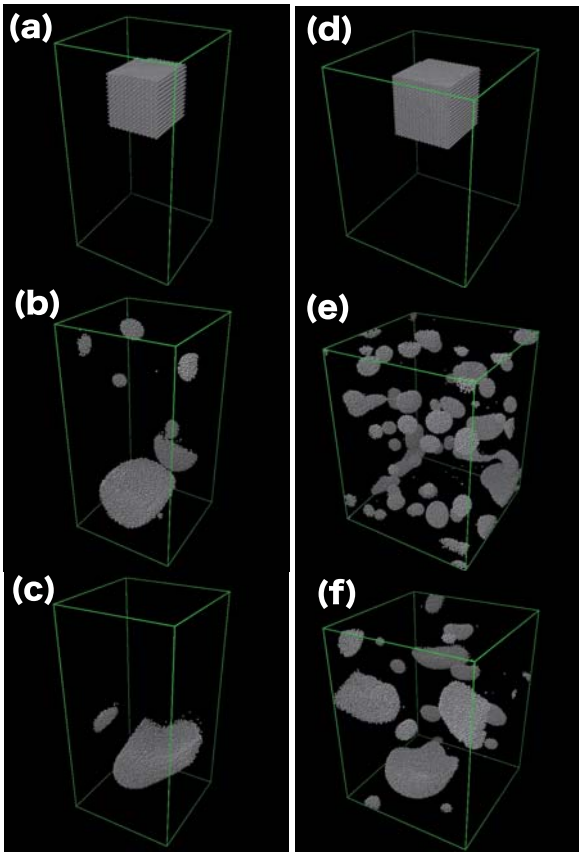

Figure 9. Case 3D4. Falling metal droplet (white) in silicate liquid (clear). The boundaries are periodic in all directions. An initially cubic drop is transformed into a spherical cap (see Figure 10) and broken up by viscous stress. In case 3D1 (Figures 9a–9c) and case 3D4 (Figures 9d–9f), the only difference between the two being the domain size: (a) 0 s, (b) 1.2 s, (c) 7.0 s, (d) 0 s, (e) 2.0 s, and (f) 4.3 s. Movie 2 is also for case 3D4.

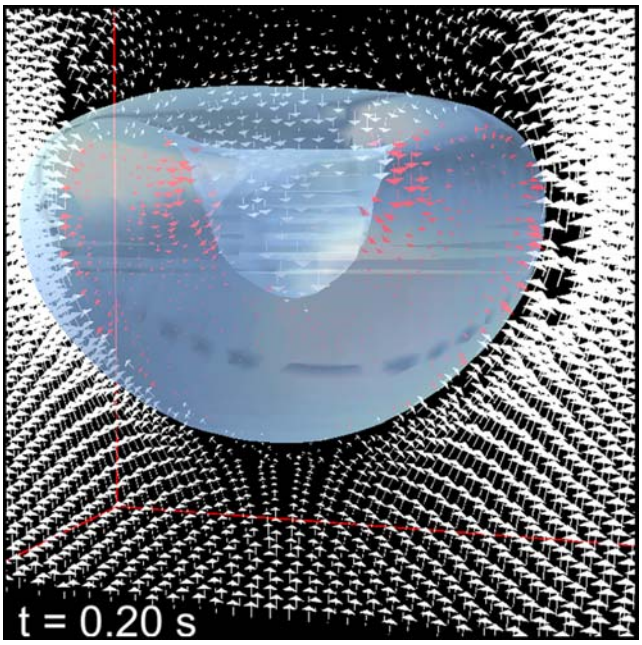

Figure 10. Deformation of a spherical drop into a spherical cap before disruption in smaller droplets, corresponding to a frame between that of Figures 9d and 9e. The surface of the drop is rendered as a blue isosurface, and the vectors represent velocity in the reference frame of the drop, in the center plane. White is for the silicates, and red is for the metal. Circulation in the silicate and the metal indents the drop from above and, eventually, leads to its break up.

recorded in mantle rocks would correspond to a sharply defined position in a P-T diagram, which would be close to the bottom of the magma ocean. In the classic cartoon of core formation proposed by *Stevenson* [1990] (Figure 1), the subsequent stages involve a rapid transfer across the solid mantle by either Rayleigh-Taylor instability, hydraulic fracturing [*Stevenson*, 2003], or percolation. In any of these processes, chemical equilibration with the mantle is hindered by slow chemical diffusion in the solid so that the last equilibrium is acquired at the bottom of the magma ocean and the present chemical composition of the mantle is thought to reflect that equilibrium. However, this interpretation seems simplistic for several reasons.

[44] The interpretation of mantle chemistry as the result of equilibration with core forming iron at a single pressure and temperature condition requires that the whole mantle gets processed by this equilibrium. However, it is now recognised that core formation occurs very early in the solar system, at the planetesimal stage [e.g. *Yin et al.*, 2002; *Baker et al.*, 2005] and on growing planets [*Ricard et al.*, 2009]. For the cartoon discussed above to keep its relevance, the last giant impacts must be able to reprocess a large fraction of the mantle by an efficient emulsification of the core of the protoplanets.

[45] The possible existence of another magma ocean at the bottom of the mantle [*Labrosse et al.*, 2007; *Mosenfelder et al.*, 2009; *Stixrude et al.*, 2009] can also affect the composition of the mantle resulting from core formation. The proportion of the falling iron that should reequilibrate with this basal magma ocean (BMO) depends on the ability of the large scale diapirs to be disrupted in centimeter-sized droplets while crossing this magma layer. This emulsification is different from that occurring upon impact at the surface since it does not benefit from any kinetic energy. The main control parameter here is the ratio between the scale of incoming iron diapirs and the thickness of the BMO, both numbers being poorly constrained.

[46] Another issue worth considering concerns the efficiency of metal segregation by the process investigated here. We have shown in this paper that a simple scaling for the size and velocity of iron drops in the magma ocean is consistent with the averaged values resulting from a full calculation. However, we have shown that the distribution in these values is rather wide and that this can even lead to very small droplets moving upward with the magma return flow. At the large scale, the volume fraction of iron depends on the position in the magma ocean and the size and velocity distributions should also depend on position. Our findings suggest that the smallest droplets would tend to be brought up by the flow due to the fall of the largest drops. We might therefore envision that the average drop size

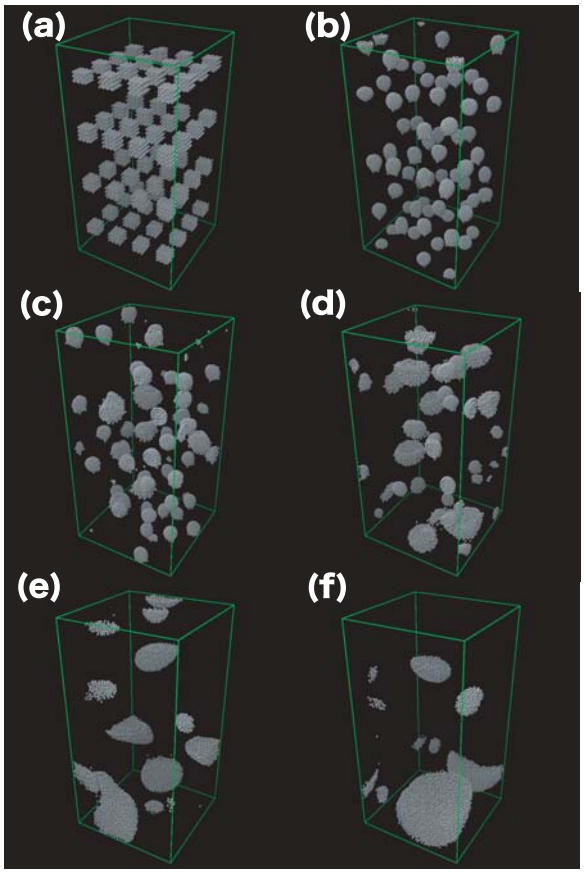

Figure 11. Case 3D2. Falling metal droplet (white) in silicate liquid (clear). The boundaries are periodic in all directions. Sixty-four initially cubic drops are positioned at lattice points: (a) 0 s, (b) 0.8 s, (c) 3.0 s, (d) 4.0 s, (e) 6.0 s, and (f) 7.8 s. The initial cubic shape is still apparent as sharp angles under the droplets in Figure 11b. Movie 3 is also for this case.

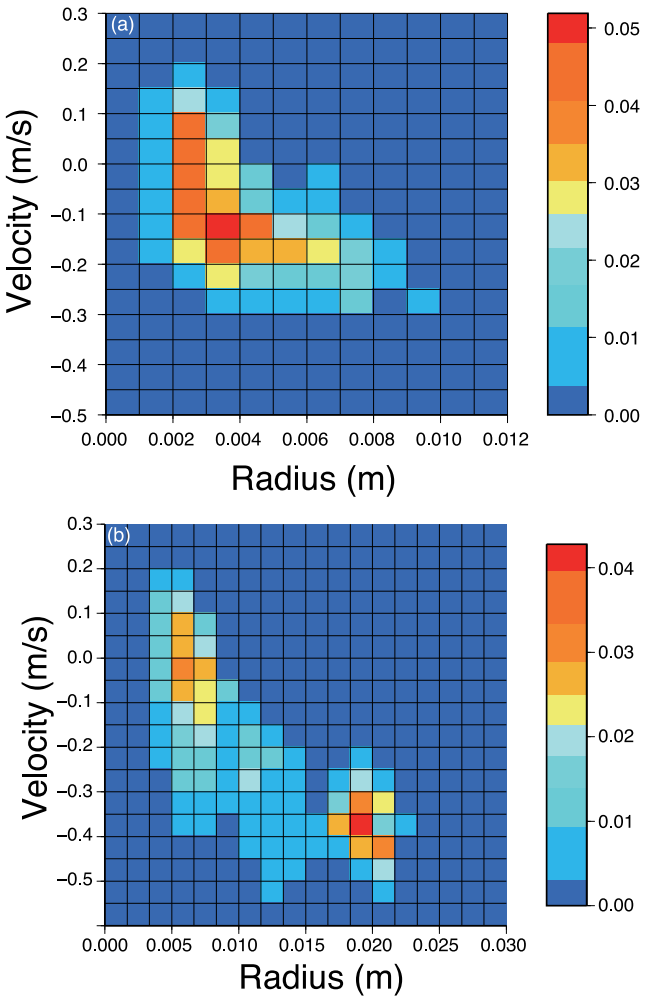

Figure 12. Volume distribution of size and velocity of droplets in statistical steady state in (a) a two-dimensional calculation (case A4) and (b) a three-dimensional (case 3D4). Both spatial and temporal variabilities are considered in the statistics.

would be lower at the top than at the bottom of the magma ocean. In particular, the smallest droplets at the top of the emulsion might be entrained by convection in the magma ocean. In this case, some metal could be left behind core formation and stay in the mantle after its solidification.

[47] In order to investigate the importance of that phenomenon, we can use the criterion proposed by *Solomatov and Stevenson* [1993] which deals with the entrainment by thermal convection of settling crystals at the bottom of the magma ocean. The negative buoyancy in the case of iron droplets is much larger so that, for an equal particle size, the maximum fraction that can be kept suspended is much smaller. For the smallest droplets of radius 5×10^{-3} m found in three-dimensional calculations (Figure 12), the maximum fraction allowing suspension is found by assuming the largest heat flow, about $q \sim 10^5$ J m^{-2} s^{-1} [*Solomatov and Stevenson*, 1993], a large viscosity $\eta = 1$ Pa s and the maximum fraction of iron that can be suspended is $\phi_{\max} = 6 \times 10^{-6}\ \varepsilon$, $\varepsilon \sim 0.01$ being the fraction of the available work from thermal convection that is used to maintain the emulsion. The resulting number is vanishingly small which shows that the process of iron rain in the magma ocean is extremely efficient.

[48] **Acknowledgments.** The authors thank Sash Hier-Majumder, an anonymous reviewer and the editors for their comments that helped to sharpen the paper. Part of the calculations presented here were performed using the facilities of the Pôle Scientifique de Modélisation Numérique (PSMN, ENS Lyon). Hiroki Ichikawa has been supported as a JSPS research fellow and then by ANR BEGDy and the Rhone-Alpes program CIBLE during this work. Stéphane Labrosse benefited from grants of "Predictability of the Evolution and Variation of the Multiscale Earth System: An integrated COE for Observational and Computational Earth Science" to visit the University of Tokyo and the Earthquake research institute. The authors wish to thank the support of the COE's internship by the university of Tokyo. This work was also supported by ANR program DynBMO.

References

Baker, J. A., M. Bizzarro, N. Wittig, J. Connelly, and H. Haack (2005), Early planetesimal melting from an age of 4.5662 Gyr for differentiated meteorites, *Nature*, *436*, 1127–1131, doi:10.1038/nature03882.

Bercovici, D., Y. Ricard, and G. Schubert (2001), A two-phase model for compaction and damage. 1. General theory, *J. Geophys. Res.*, *106*, 8887–8906, doi:10.1029/2000JB900430.

Boyet, M., J. Blichert-Toft, M. Rosing, M. Storey, P. Telouk, and F. Albarede (2003), Nd-142 evidence for early Earth differentiation, *Earth Planet. Sci. Lett.*, *214*(3–4), 427–442, doi:10.1016/S0012-821X(03)00423-0.

Brackbill, J. U., D. B. Kothe, and C. Zemach (1992), A continuum method for modeling surface tension, *J. Comput. Phys.*, *100*, 335–354, doi:10.1016/0021-9991(92)90240-Y.

Bruhn, D., N. Groebner, and D. L. Kohlstedt (2000), An interconnected network of core-forming melts produced by shear deformation, *Nature*, *403*, 883–886, doi:10.1038/35002558.

Canup, R. M. (2004), Simulations of a late lunar-forming impact, *Icarus*, *168*, 433–456, doi:10.1016/j.icarus.2003.09.028.

Caro, G., B. Bourdon, J.-L. Birck, and S. Moorbath (2003), ^{146}Sm-^{142}Nd evidence from Isua metamorphosed sediments for early differentiation of the Earth's mantle, *Nature*, *423*, 428–432, doi:10.1038/nature01668.

Caro, G., B. Bourdon, B. J. Wood, and A. Corgne (2005), Trace-element fractionation in Hadean mantle generated by melt segregation from a magma ocean, *Nature*, *436*, 246–249, doi:10.1038/nature03827.

Clift, R., J. R. Grace, and M. E. Weber (1978), *Bubbles, Drops and Particles*, Dover, New York.

Drew, D. A. (1983), Mathematical modeling of two-phase flow, *Annu. Rev. Fluid Mech.*, *15*(1), 261–291, doi:10.1146/annurev.fl.15.010183.001401.

Eggers, J., J. R. Lister, and H. A. Stone (1999), Coalescence of liquid drops, *J. Fluid Mech.*, *401*, 293–310, doi:10.1017/S002211209900662X.

Golabek, G. J., H. Schmeling, and P. J. Tackley (2008), Earth's core formation aided by flow channelling instabilities induced by iron diapirs, *Earth Planet. Sci. Lett.*, *271*(1–4), 24–33, doi:10.1016/j.epsl.2008.02.033.

Honda, R., H. Mizutani, and T. Yamamoto (1993), Numerical simulation of Earth's core formation, *J. Geophys. Res.*, *98*, 2075–2089, doi:10.1029/92JB02699.

Ichikawa, H., and S. Labrosse (2010), Smoothed particle approach for surface tension calculation in moving particle semi-implicit method, *Fluid Dyn. Res.*, in press.

Jaupart, C., S. Labrosse, and J.-C. Mareschal (2007), Temperatures, heat and energy in the mantle of the Earth, in *Treatise of Geophysics*, vol. 7, *Mantle Dynamics*, pp. 253–303, Elsevier, New York.

Karato, S., and V. Rama Murthy (1997), Core formation and chemical equilibrium in the Earth. 1. Physical considerations, *Phys. Earth Planet. Inter.*, *100*(1–4), 61–79, doi:10.1016/S0031-9201(96)03232-3.

Koshizuka, S., and Y. Oka (1996), Moving-particle semi-implicit method for fragmentation of incompressible fluid, *Nucl. Sci. Eng.*, *123*, 421–434.

Koshizuka, S., H. Ikeda, and Y. Oka (1999), Numerical analysis of fragmentation mechanisms in vapor explosions, *Nucl. Eng. Des.*, *189*, 423–433, doi:10.1016/S0029-5493(98)00270-2.

Labrosse, S., and C. Jaupart (2007), Thermal evolution of the Earth: Secular changes and fluctuations of plate characteristics, *Earth Planet. Sci. Lett.*, *260*, 465–481, doi:10.1016/j.epsl.2007.05.046.

Labrosse, S., J. W. Hernlund, and N. Coltice (2007), A crystallizing dense magma ocean at the base of Earth's mantle, *Nature*, *450*, 866–869, doi:10.1038/nature06355.

Li, J., and C. B. Agee (1996), Geochemistry of mantle-core differentiation at high pressure, *Nature*, *381*, 686–689, doi:10.1038/381686a0.

Liebske, C., B. Schmickler, H. Terasaki, B. T. Poe, A. Suzuki, K. Funakoshi, R. Ando, and D. C. Rubie (2005), Viscosity of peridotite liquid up to 13 GPa: Implications for magma ocean viscosities, *Earth Planet. Sci. Lett.*, *240*(3–4), 589–604, doi:10.1016/j.epsl.2005.10.004.

Mosenfelder, J. L., P. D. Asimow, D. J. Frost, D. C. Rubie, and T. J. Ahrens (2009), The $MgSiO_3$ system at high pressure: Thermodynamic properties of perovskite, postperovskite, and melt from global inversion of shock and static compression data, *J. Geophys. Res.*, *114*, B01203, doi:10.1029/2008JB005900.

Nomura, K., S. Koshizuka, Y. Oka, and H. Obata (2001), Numerical analysis of droplet breakup behavior using particle method, *J. Nucl. Sci. Technol.*, *38*, 1057–1064, doi:10.3327/jnst.38.1057.

Ricard, Y., O. Šrámek, and T. Dubuffet (2009), A multi-phase model of runaway core-mantle segregation in planetary embryos, *Earth Planet. Sci. Lett.*, *28*(1–2), 144–150, doi:10.1016/j.epsl.2009.04.021.

Rubie, D. C., H. J. Melosh, J. E. Reid, C. Liebske, and K. Righter (2003), Mechanisms of metal-silicate equibration in the terrestrial magma ocean, *Earth Planet. Sci. Lett.*, *205*, 239–255, doi:10.1016/S0012-821X(02)01044-0.

Samuel, H., and P. J. Tackley (2008), Dynamics of core formation and equilibration by negative diapirism, *Geochem. Geophys. Geosyst.*, *9*, Q06011, doi:10.1029/2007GC001896.

Scardovelli, R., and S. Zaleski (1999), Direct numerical simulation of free-surface and interfacial flow, *Annu. Rev. Fluid Mech.*, *31*(1), 567–603, doi:10.1146/annurev.fluid.31.1.567.

Solomatov, V. S., and D. J. Stevenson (1993), Suspension in convective layers and style of differentiation of a terrestrial magma ocean, *J. Geophys. Res.*, *98*, 5375–5390, doi:10.1029/92JE02948.

Stevenson, D. J. (1990), Fluid dynamics of core formation, in *Origin of the Earth*, edited by H. E. Newsom and J. H. Jones, pp. 231–249, Oxford Univ. Press, New York.

Stevenson, D. J. (2003), Mission to Earth's core—A modest proposal, *Nature*, *423*, 239–240, doi:10.1038/423239a.

Stixrude, L., N. de Koker, N. Sun, M. Mookherjee, and B. B. Karki (2009), Thermodynamics of silicate liquids in the deep Earth, *Earth Planet. Sci. Lett.*, *278*(3–4), 226–232, doi:10.1016/j.epsl.2008.12.006.

Thibault, Y., and M. J. Walter (1995), The influence of pressure and temperature on the metal-silicate partition coefficients of nickel and cobalt in a model C1 chondrite and implications for metal segregation in a deep matma ocean, *Geochim. Cosmochim. Acta*, *59*, 991–1002, doi:10.1016/0016-7037(95)00017-8.

Tonks, W. B., and H. J. Melosh (1990), The physics of crystal settling and suspension in a turbulent magma ocean, in *Origin of the Earth*, edited by H. E. Newsom and J. Jones, pp. 151–174, Oxford Univ. Press, New York.

Tonks, W. B., and H. J. Melosh (1993), Magma ocean formation due to giant impacts, *J. Geophys. Res.*, *98*, 5319–5333, doi:10.1029/92JE02726.

Wood, B. J., M. J. Walter, and J. Wade (2006), Accretion of the Earth and segregation of its core, *Nature*, *441*, 825–833, doi:10.1038/nature04763.

Yin, Q. Z., S. B. Jacobsen, K. Yamashita, J. Blichert-Toft, P. Telouk, and F. Albarede (2002), A short timescale for terrestrial planet formation from Hf-W chronometry of meteorites, *Nature*, *418*, 949–952, doi:10.1038/nature00995.

Yoshino, T., M. J. Walter, and T. Katsura (2003), Core formation in planetesimals triggered by permeable flow, *Nature*, *422*, 154–157, doi:10.1038/nature01459.

H. Ichikawa, Geodynamics Research Center, Ehime University, 2-5 Bunkyo-cho, Matsuyama 790-8577, Japan. (h-ichikawa@sci.ehime-u.ac.jp)

K. Kurita, Earthquake Research Institute, University of Tokyo, 1-1-1, Yayoi, Bunkyo-ku, Tokyo, Japan. (kurikuri@eri.u-tokyo.ac.jp)

S. Labrosse, Laboratoire des sciences de la Terre, École Normale Supérieure de Lyon, 46 Allée d'Italie, F-69364 Lyon CEDEX 07, France. (stephane.labrosse@ens-lyon.fr)